

Design of S-band photoinjector with high bunch charge and low emittance based on multi-objective genetic algorithm

Ze-Yi Dai¹, Yuan-Cun Nie^{1*}, Zi Hui¹, Lan-Xin Liu¹, Zi-Shuo Liu¹, Jian-Hua Zhong¹, Jia-Bao Guan¹, Ji-Ke Wang¹, Yuan Chen¹, Ye Zou¹, Hao-Hu Li¹, Jian-Hua He^{1**}

¹ *The Institute for Advanced Studies, Wuhan University, Wuhan 430072, China*

* Corresponding author *E-mail address:* nieyuancun@whu.edu.cn

** Corresponding author *E-mail address:* hejianhua@whu.edu.cn

Abstract

High-brightness electron beams are required to drive LINAC-based free-electron lasers (FELs) and storage-ring-based synchrotron radiation light sources. The bunch charge and RMS bunch length at the exit of the LINAC play a crucial role in the peak current; the minimum transverse emittance is mainly determined by the injector of the LINAC. Thus, a photoinjector with a high bunch charge and low emittance that can simultaneously provide high-quality beams for 4th generation synchrotron radiation sources and FELs is desirable. The design of a 1.6-cell S-band 2998-MHz RF gun and beam dynamics optimization of a relevant beamline are presented in this paper. Beam dynamics simulations were performed by combining ASTRA and the multi-objective genetic algorithm NSGA II. The effects of the laser pulse shape, half-cell length of the RF gun, and RF parameters on the output beam quality were analyzed and compared. The normalized transverse emittance was optimized to be as low as 0.65 and 0.92 mm·mrad when the bunch charge was as high as 1 and 2 nC, respectively. Finally, the beam stability properties of the photoinjector, considering misalignment and RF jitter, were simulated and analyzed.

Keywords Electron linear accelerator; Photoinjector; Beam dynamics; Multi-objective genetic algorithm

1. Introduction

The LINAC-based free-electron laser (FEL) and storage-ring-based diffraction limited storage ring (DLSR) have become important tools for exploring the microscopic world, promoting the development of physics, chemistry, biology, materials, and related fields [1-5]. Normal conducting RF (NCRF) photoinjectors are widely used in FELs for their low emittance and high brightness, as shown in Table 1. The development of synchrotron radiation sources has gone through three generations. The 4th generation synchrotron radiation source based on

DLSR has become a new trend; the brightness is 2-3 orders of magnitude greater than that of the third generation [13]. After the great success achieved by MAX-IV in Sweden [14], Sirius in Brazil completed the first phase of commissioning [15]. In addition, a series of 4th generation synchrotron radiation sources are under construction or in the planning stage, including APS-U, SPring-8, ALS, Soleil, Diamond, HEPS, and HALS [16]. Although thermal cathode injectors have been widely used in synchrotron light sources [17], photoinjectors have become a better choice when higher beam brightness is required from the LINAC; S-band photoinjectors are used at MAX-IV, HALF, etc. [18, 19].

Table 1 Application of NCRF photoinjector in FELs

FEL	SXFEL [6,7]	LCLS [8]	Pal-XFEL [9,10]	Swiss-FEL [11,12]
Gun type	1.6-cell	1.6-cell	1.6-cell	2.5-cell
Bunch charge (nC)	0.5	0.25	0.2	0.2
Peak current (A)	62.5	35	~30	20
Projected emittance (mm·mrad)	0.8-0.9	0.5	0.35	0.3

In this study, a dual-use photoinjector is described that can provide high-quality beams for either the storage ring, where a high bunch charge of more than 1 nC is required in the swap-out injection mode, or the FEL, where a low emittance is preferred [20-22]. Swap-out injection is a potential alternative for beam injection at DLSRs, where off-axis cumulative injection can become too difficult due to the small dynamic apertures.

In beam dynamics optimization of photoinjectors, the approximate range of parameters can be obtained by theoretical analysis; however, to obtain more accurate results, optimization algorithms based on theoretical guidance are often required. For multiparameter optimization in accelerator applications, the multi-objective genetic algorithm (MOGA) and multi-objective particle swarm algorithm (MOPSO) are mainstream algorithms [23-30]. The former has a fast convergence rate, whereas the latter can generate more diversity in the solution space and has a strong global searching ability. In our study with eight variables, MOGA based on the non-dominated sorting genetic algorithm-II (NSGA-II) is a reliable algorithm [31]; it reduces the complexity of the non-dominated sorting genetic algorithm and has the advantage of fast running speed and good convergence performance.

The design of the 1.6-cell S-band 2998-MHz RF gun and the beam dynamics optimization of the photoinjector are presented in detail. The RF design of the gun is discussed in Section 2; the main purpose is to create a flat axial field distribution, large separation between adjacent

electromagnetic modes, and a higher axial field than that on the cavity surface. In Section 3, beam dynamics optimization is carried out using NSGAII and ASTRA considering different laser pulse shapes, half-cell lengths of the gun, and RF gradients. In Section 4, a stability analysis of the photoinjector is presented after introducing misalignment and RF jitter.

2. RF design

A 1.6-cell S-band BNL/SLAC/UCLA photocathode RF gun is described in this section [32]. The gun performance was improved by optimizing the Q factor, peak electric field on the cavity wall, adjacent mode separation, and axis electric field flatness. Electromagnetic field calculations were performed using SUPERFISH [33], which can quickly adjust the frequency to the set point, balance the axial electric field between the half-cell and the full-cell, and provide a field map for beam dynamics simulations.

In the optimization process, the ratio of the peak electric field on the wall E_{\max} to the field on the photocathode E_c can be reduced using an elliptic iris instead of a circular iris. Another parameter that must be optimized is the separation between adjacent modes. Both the 0-mode and π -mode are present in the RF gun. The 0-mode cannot accelerate the electron beam, leading to emittance growth and additional energy spread [34]. Thus, the distance between the 0-mode and π -mode should be increased by increasing the iris aperture or decreasing the disk thickness. Fig. 1 shows the influence of the iris aperture r_a and axial ratio $t=t_a/t_b$ on the RF parameters. As shown in Fig. 1(b), if the major and minor axes of the elliptic iris are fixed at $t_a=16$ mm and $t_b=10$ mm, the distance between the 0-mode and π -mode increases rapidly from 5 MHz to 75 MHz when r_a expands from 11 mm to 20 mm, and the Q factor increases by 4%. The effect of the axial ratio is shown in Fig. 1(c). When the aperture $r_a=18$ mm and minor axis $t_b=10$ mm were unaltered, E_{\max} decreased from 5% higher than E_c to 8% lower than E_c ; the mode separation increased from 40 MHz to 49 MHz as the major axis t_a increased from 10 mm to 16 mm.

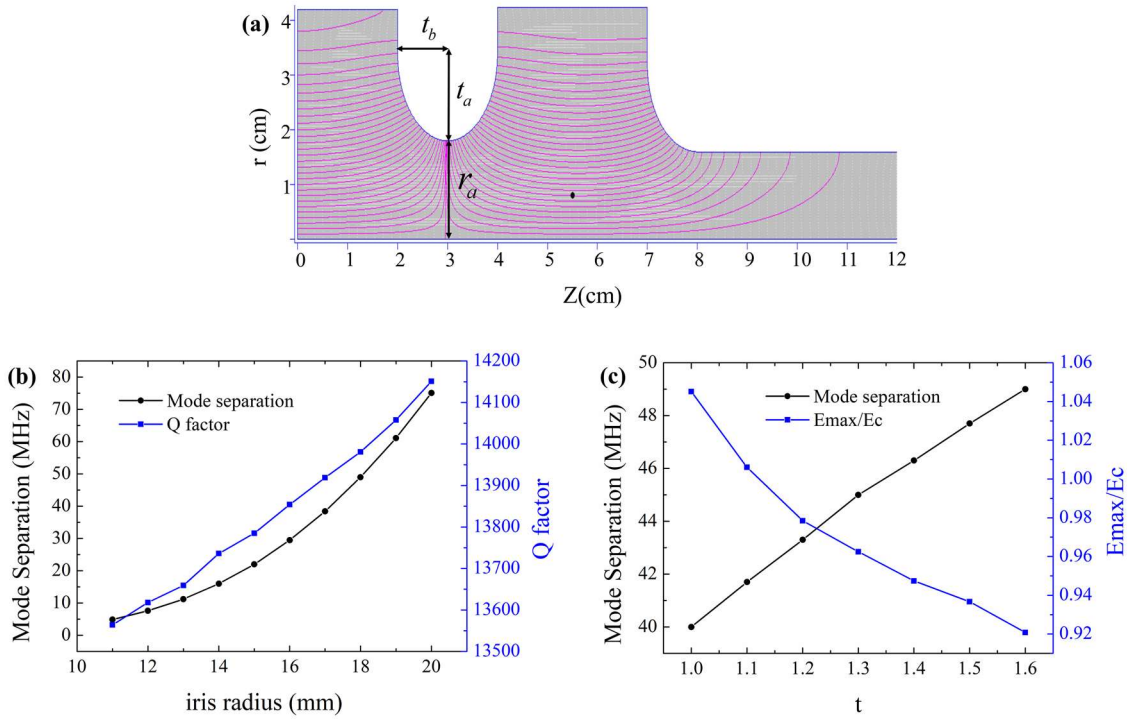
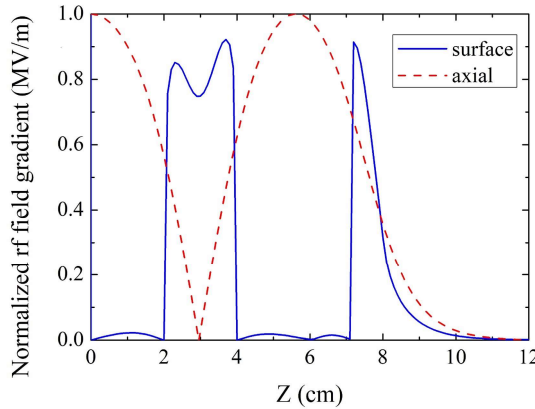


Fig. 1 RF optimization of the gun: (a) Electric field distribution of 1.6-cell RF gun in π mode; (b) RF parameters at $t_a=16$ mm and $t_b=10$ mm; (c) RF parameters at $r_a=18$ mm and $t_b=10$ mm

The distance between 0-mode and π -mode was increased from 3.5 to 15 MHz by optimizing the cavity structure in the LCLS RF gun [35]. Consequently, the amplitude of the 0-mode electric field on the photocathode decreased from 10% of the axial field to less than 3%, and the beam performance was significantly improved. A larger frequency separation (>40 MHz) between the two resonant modes further limits the excitation of the 0-mode during transients in the pulsed regime. Thus, a uniform accelerating field can be obtained along the bunch train, and the field gradient variation on the photocathode can be controlled to approximately 0.1%, which is particularly important for beams with short pulses and high repetition frequencies [36]. The final working point was selected as $t_a=16$ mm, $t_b=10$ mm, and $r_a=18$ mm. The optimized RF gun parameters are listed in Table 2. The relationship between the normalized axial electric field and surface field along the axis is shown in Fig. 2. The field flatness (field ratio between the half cell and full cell) was 1, and the electric field on the cavity surface was lower than that on the axis. The axial electric field map can be extracted from SUPERFISH as an input file for beam dynamics optimization using ASTRA [37].

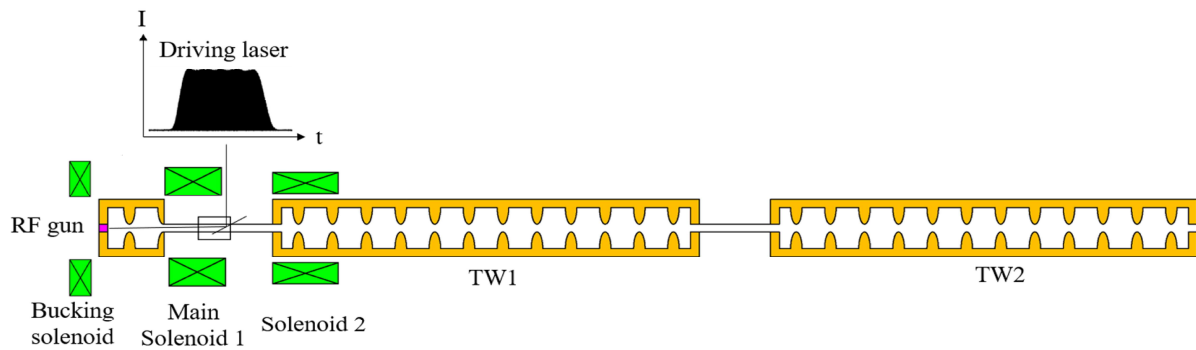
Table 2 Main parameters of S-band RF gun

RF parameter	value
f_π (MHz)	2997.99
Q_0	13474
Mode Sep. Δf (MHz)	49
Field flatness	1
E_{\max}/E_c	0.921

**Fig. 2** Electric field distribution on cavity surface and on axis of RF gun

3. Beam dynamics

An S-band photoinjector system typically consists of a driving laser, a photocathode RF gun, and focusing solenoids, as shown in Fig. 3. The laser pulse from the drive-laser system stimulates the photocathode to generate electron beams. In the gun, a high-gradient RF field rapidly accelerates the beams emitted at the photocathode to a relativistic velocity. The solenoids focus the beam transversely and align the slice distribution of the bunch in the transverse phase space to compensate for the emittance growth owing to linear space charge forces [38]. With the help of the following acceleration tubes, the beam becomes highly relativistic at the end of the injector, and the space charge effect no longer causes significant emittance growth.

**Fig. 3** Layout of S-band photoinjector

Ideally, a beam with a shorter bunch length, lower emittance, smaller transverse size, and lower energy spread is expected. The beam quality is determined by many parameters, including the transverse and temporal profile of the laser pulse, the RF field gradient and phase of the photocathode gun, the magnetic field strength excited by the solenoids, the RF gradient, and the phase of the accelerating cavities. The energy spread is primarily determined by the RF phase in the S-band traveling wave (TW) accelerating cavity under the same initial bunch length. A minimum energy spread can be obtained at the exit of the injector as long as the RF phase is close to the on-crest phase. The transverse beam size can be easily adjusted by focusing elements such as quadrupoles. The main optimization objective is thus to reduce the Root-Mean-Squared (RMS) bunch length and normalized transverse emittance.

To improve the simulation process, the multi-objective genetic algorithm NSGAII combined with ASTRA code was used to find the optimal solution. The main optimization objectives are the RMS bunch length and normalized transverse emittance, both of which are expected to be as low as possible to improve the beam brightness. The constraints of the output RMS transverse bunch size and relative energy spread were added in the optimization process to ensure beam quality and transmission efficiency. A driving laser pulse with a plateau temporal distribution was used; the full-width-at-half-magnitude (FWHM) pulse length was 10 ps, and the rise/fall time of the pulse was 1 ps. Initial bunch charges of 1 nC and 2 nC were studied. The purpose of the bucking solenoid is to obtain a vanishing magnetic field at the cathode by introducing a current opposite to the main solenoid, which would otherwise introduce emittance growth owing to the initially magnetized beam [34]. The emittance contribution owing to the magnetized beam was estimated to be less than 0.003 mm·mrad for a magnetic field of 8 G in our simulation, which does not affect the final optimization result. The intrinsic thermal emittance of the photocathode material was set as 0.9 mm·mrad/mm, referring to the measurement results of the metal photocathode at the LCLS and the values of semiconductor materials [39, 40]. To compromise between running time and accuracy, 10k macro-particles were used in beam dynamics simulations. The space charge fields were calculated on a cylindrical grid, consisting of 20 rings in the radial direction and 30 slices in the longitudinal direction; the maximum time step was set as 1 ps. The time required for one cycle in ASTRA was approximately 7 min. The population size of each generation was set as 120; the total number of runs was 100, and 90 particle files were run simultaneously using parallel computations. The interesting solutions were re-simulated with 100k macro-particles in ASTRA for a more detailed analysis.

3.1. Beam dynamics simulation at 1 nC

The emittance compensation technique using focusing solenoids is an effective way to minimize emittance growth owing to space charge forces; however, it can only compensate for the emittance growth caused by the linear space charge force. In reality, the nonlinear space-charge force can also cause additional emittance growth. Theoretical analysis and experiments prove that the flat-top temporal distribution and transversely truncated Gaussian distribution with approximately 1 sigma truncation can linearize the space-charge effect [41]. The transverse laser profile can be shaped by a beam-shaping aperture (BSA) along the transport beamline from the laser to the photocathode. Truncated Gaussian distributions with truncated ratios of 0.9/1.1/1.5 sigma are shown in Fig. 4. The parameter variables in the beam dynamics optimization based on NSGAII are listed in Table 3; the range is narrowed from the optimization with a larger scanning domain. A higher RF field gradient can accelerate the bunch to relativistic velocity more rapidly, which can suppress emittance growth and beam expansion caused by the space-charge effect. To obtain a bunch charge greater than 1 nC, Cs₂Te semiconductor photocathodes are preferred. The operating RF field gradient must be as low as possible to prolong the photocathode lifetime [42]. To compromise between the bunch charge and RF field gradient, the gradient was set to 100 MV/m.

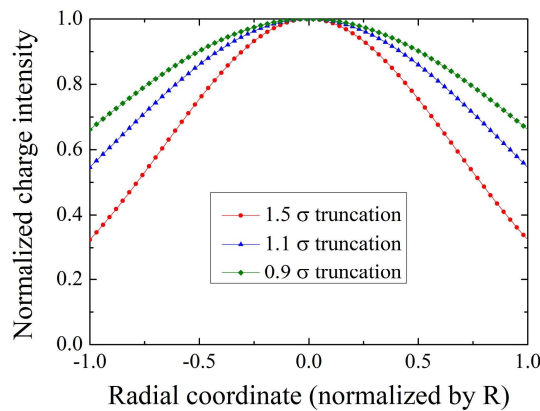


Fig. 4 Transverse truncated Gaussian distributions with truncated ratios of 0.9, 1.1, and 1.5 σ

Table 3 Main parameters for beam dynamics optimization

Decision variable	Optimization range
σ (rms value before Gaussian truncation)	0.4 ~ 2.0 mm
Gun phase	-30°~30°
TW1 start position ^a	1 ~2 m
TW1 field gradient	15 ~ 27 MV/m
Distance between two TW cavities	1 ~ 2 m
TW 2 field gradient	15 ~ 27 MV/m
Main solenoid1 field	0.1 ~ 0.4 T
Solenoid2 field	0.01 ~ 0.2 T
<hr/>	
Objective	Goal
RMS bunch length	Minimize
Normalized transverse emittance	Minimize
<hr/>	
Constraint	Range
Output RMS transverse bunch size	< 1.0 mm
Output relative energy spread	< 0.5%

^a Distance from surface of photocathode

The obtained Pareto front composed of non-dominant solutions is shown in Fig. 5(a), and demonstrates the equilibrium relationship between the normalized transverse emittance and RMS bunch length. In addition, truncated Gaussian distributions with different truncated ratios of 0.8/1.0/1.2/2.0 sigma were simulated. The achievable minimum emittance and corresponding beam size after truncation as a function of the truncation ratio are shown in Fig. 5(b). The optimal normalized transverse emittance with beam truncation at 1 sigma and 1.5 sigma is 0.61 mm·mrad and 0.65 mm·mrad, respectively. For a 1.5 sigma truncation, although the achievable minimum emittance is slightly higher, the utilization efficiency of the driving laser power is greatly improved compared with a 1 sigma truncation. The laser efficiency is important to realize a high initial bunch charge; thus, a transversely Gaussian distribution with the radius truncated at 1.5 sigma was selected for subsequent simulations. According to Dowell's theory [43], for the pancake beam, considering the mirror charge field of the bunch, the thermal emittance can be expressed as

$$\varepsilon = \sigma_{x,y} \sqrt{\frac{\hbar\omega - \phi_w + e\sqrt{e(E_0 \sin \phi - \frac{Q}{\varepsilon_0 S})/4\pi\varepsilon_0}}{3mc^2}} \quad (1)$$

where $\sigma_{x,y}$ is the initial RMS transverse size; $\hbar\omega$ is the photon energy of the laser; ϕ_w is the working function; $E_0 \sin \phi$ is the electric field on the photocathode during photoemission. Assuming the initial bunch has a 2D radial uniform distribution, the thermal emittance is minimized as long as the beam radius meets the condition $Q = \pi r^2 \varepsilon_0 E_0 \sin \phi$. After optimization, for the 1.6-cell S-band RF gun, the electric field during photoemission is approximately 41 MV/m; the optimal beam radius for minimum thermal emittance is calculated as 0.94 mm, equivalent to an initial RMS beam size of 0.47 mm. This theoretical result is consistent with the simulation results shown in Fig. 5(b) at different Gaussian truncation ratios.

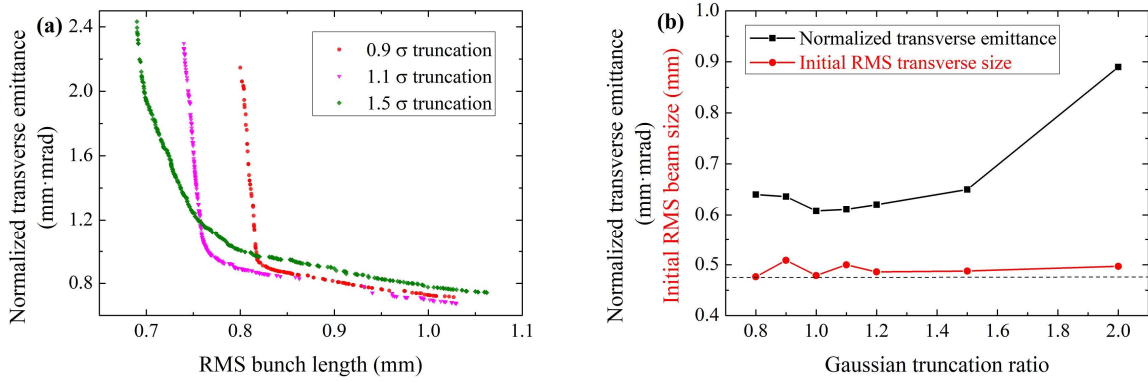


Fig. 5 Multi-objective optimization results for injector at 1 nC: (a) Multi-objective optimization results for 0.9/1.1/1.5 sigma truncation; (b) Minimum emittance and corresponding beam size (after truncation) at different Gaussian truncation ratios

An RMS bunch length of 1.04 mm and a transverse Gaussian with radius truncated at 1.5 sigma were set as the working points, and 100k macro-particles were simulated. In Fig. 6, the normalized transverse emittance is 0.65 mm·mrad with a peak current of 100 A. The 95% projected emittance is 0.56 mm·mrad, which is close to the slice emittance displayed in Fig. 7. The bunch mismatch factor is 1.09, close to 1.0.

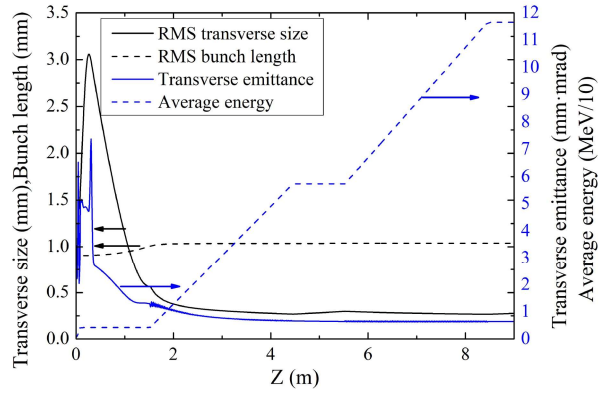


Fig. 6 Evolution of normalized transverse emittance, RMS transverse size, average energy, and RMS bunch length along the photoinjector

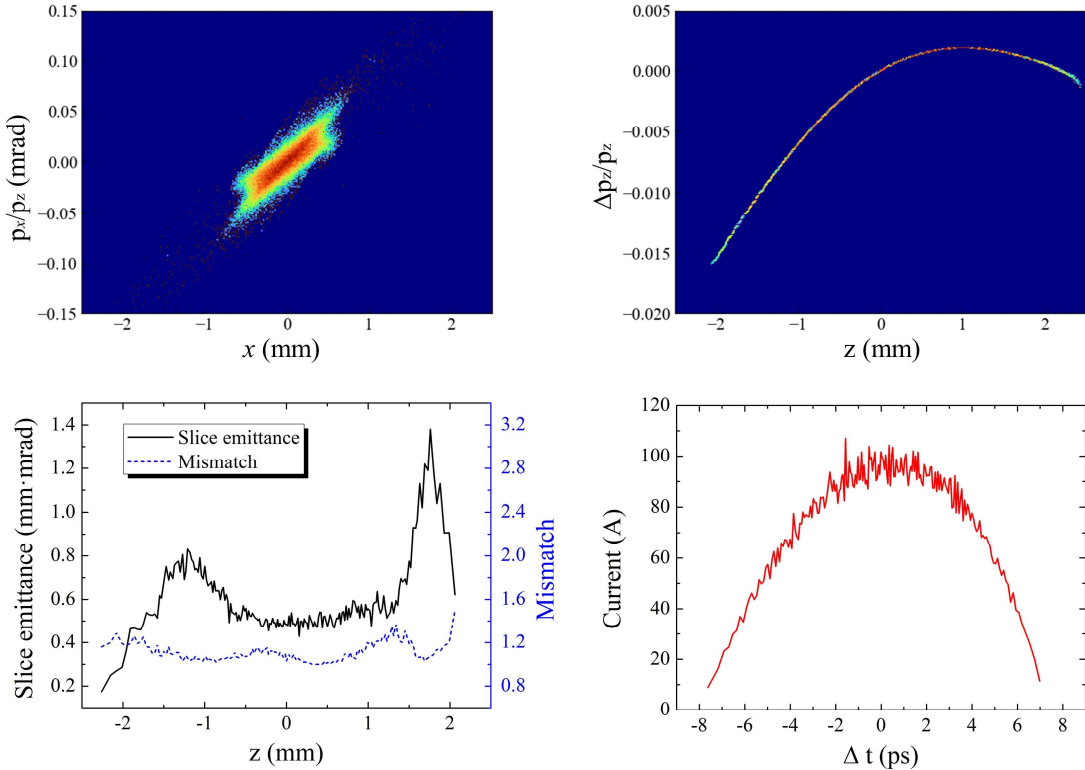


Fig. 7 Beam parameters after optimization at 1 nC: Transverse phase space (upper left), longitudinal phase space (upper right), slice emittance and mismatch (lower left), and current distribution (lower right)

3.2. Beam dynamics simulation at 2 nC

When a storage ring operates in the swap-out injection mode, a high bunch charge from the injector is essential to increase the average current in the ring. For example, at Wuhan Photon Source (WHPS), which is under design, the 1.5-GeV storage ring requests a bunch charge up

to 1.7 nC from the LINAC injector to reach the final design current of 500 mA in case of swap-out injection. A normalized transverse emittance less than 5 mm·mrad and relative energy spread lower than 0.3% at the exit of the LINAC are required. In addition, a normalized transverse emittance of less than 1 mm·mrad is expected in the planned FEL [44]. In this section, beam dynamics optimization with an initial bunch charge of 2 nC is investigated. The positions of the RF gun, solenoids, and TW structures were fixed according to the optimization results for 1 nC. The initial laser pulse with a plateau temporal distribution of 10 ps FWHM and 1 ps rise/fall time was kept the same as that for 1 nC, and the transverse Gaussian distribution was truncated at 1.5 sigma. Beam dynamics optimizations through adjustment of the laser phase, initial beam size, RF field gradient and phase, and magnetic field strength of the solenoids were performed using NSGAII. Fig. 8 shows that the initial beam size should be approximately 0.696 mm to achieve the minimum output emittance, which is consistent with the value calculated by $Q = \pi r^2 \varepsilon_0 E_0 \sin \phi$.

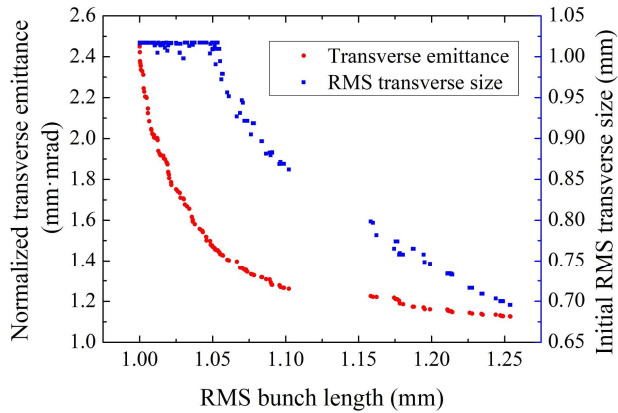


Fig. 8 Multi-objective optimization results for emittance and corresponding initial beam size (RMS value after 1.5σ truncation) as a function of output bunch length

From the optimization, the working point was chosen such that the initial RMS beam size was 0.696 mm and the output bunch length was 1.25 mm. The number of macro-particles was increased to 100k to improve the simulation accuracy. Fig. 9 shows that the normalized transverse emittance is as low as 0.92 mm·mrad with a peak current of 170 A at the exit of the photoinjector. The results indicate that injecting bunch charges as high as 2 nC with very low emittance into a storage ring using a full-energy LINAC injector with a photocathode RF gun is promising.

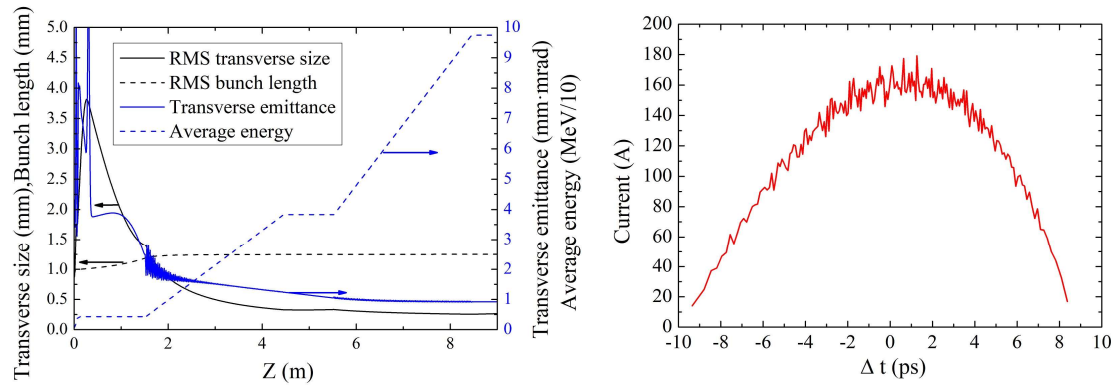


Fig. 9 Beam parameters after optimization at 2 nC

3.3. Comparison of first-cell lengths in the gun

In theory, the first-cell length in the gun is usually assumed to be 0.25λ [45], which corresponds to one-quarter period of the cosoidal temporal profile. A shorter half-cell length increases the acceleration field by putting the beam at an RF phase close to the on-crest acceleration due to less phase slippage time. The electron bunch is accelerated to relativistic velocity more rapidly, reducing the emittance growth caused by the space-charge effect [46]. However, a longer half-cell length contributes more to the longitudinal compression of the bunch and produces a greater energy gain after the half-cell. Thus, a specific optimization process is required to determine the length of the half-cell in the gun. To find the optimal length, first-cell lengths of 0.2λ and 0.3λ were studied. The simulation results are presented in Table 4. The transverse emittance and RMS bunch length varying along the photoinjector are shown in Fig. 10. The extraction field gradient at the photocathode surface of the 1.4-cell RF gun is twice that of the 1.6-cell gun, but the output beam energy at the exit of the gun is lower. The 1.6-cell gun produces a shorter output bunch length, with equivalent emittance at 1 nC and lower emittance at 2 nC.

Table 4 Optimization parameters of photoinjector with 1.4-cell gun and 1.6-cell gun

	0.2λ	0.3λ	0.2λ	0.3λ
Half-cell length				
Bunch charge (nC)	1	1	2	2
Output emittance (mm·mrad)	0.63	0.65	1.23	0.92
RMS bunch length (mm)	1.18	1.04	1.35	1.25
Energy at gun exit (MeV)	3.68	4.29	3.66	4.3
Extraction field on cathode (MV/m)	85	40.6	82.2	42.6

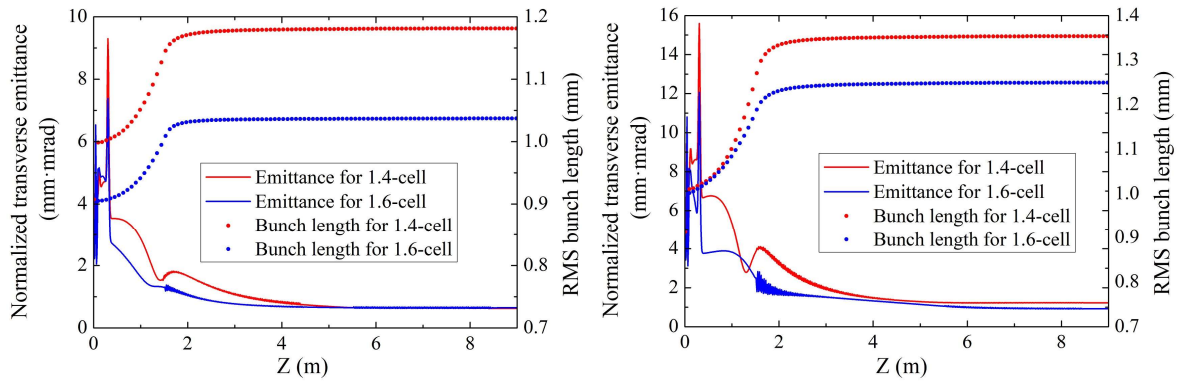


Fig. 10 Transverse emittance and bunch length varying along photoinjector with different half-cell lengths in the gun for 1 nC (left) and 2 nC (right)

3.4. Field gradient in RF gun

In general, a higher field gradient in the RF gun can more effectively suppress the emittance growth caused by the space-charge effect, leading to a lower output emittance and shorter bunch length at the exit of the photoinjector. The state-of-the-art field gradient in the S-band RF gun has reached 120 MV/m [36], with stable operation normally at approximately 100 MV/m [7]. The lifetime of semiconductor photocathode materials is largely determined by the vacuum level in the gun. The vacuum environment is sensitive to the electric field gradient; thus, the operating RF field gradient is chosen to be as low as possible. The influences of field gradients of 90 MV/m, 100 MV/m, and 120 MV/m on the beam quality at 1 nC and 2 nC were studied; the simulated results are shown in Fig. 11. For 1 nC, the minimum normalized transverse emittance was 0.83 mm·mrad, 0.74 mm·mrad, and 0.65 mm·mrad and the RMS bunch length was 0.99 mm, 1.06 mm, and 1.06 mm, respectively, as the field gradient increased from 90 MV/m to 120 MV/m. When the bunch charge was 2 nC, the corresponding minimum emittance was 1.26 mm·mrad, 1.13 mm·mrad, and 1.02 mm·mrad and the bunch length was 1.22, 1.25, and 1.18 mm, respectively. In our application, an RF gradient of 100 MV/m or even 90 MV/m could be chosen, as beam emittances as low as 0.7 and 1.0 mm·mrad could be achieved with initial bunch charges of 1 nC and 2 nC, respectively, in ASTRA simulations to meet the beam quality requirements.

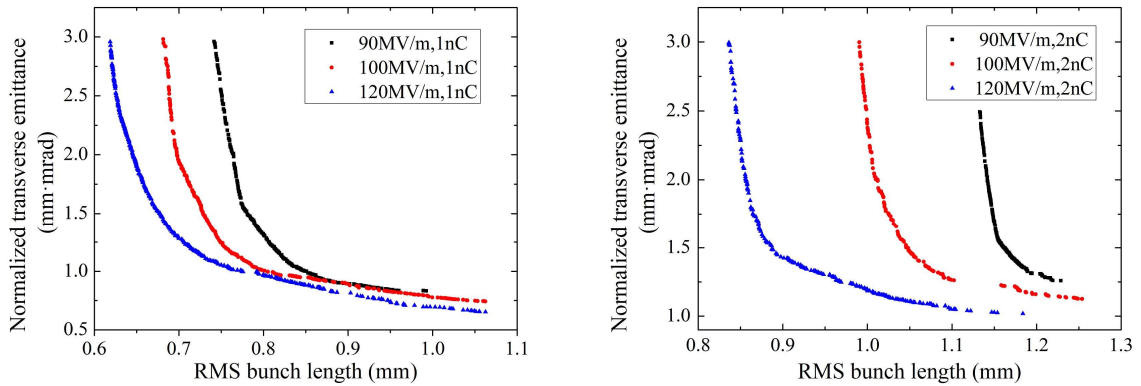


Fig. 11 Multi-objective optimization results for photoinjector with different field gradients in RF gun at 1 nC (left) and 2 nC (right)

3.5. Field flatness in RF gun

Field flatness is essential for achieving the highest possible beam energy and homogeneous RF power losses in the gun. The optimum field flatness is achieved when the maximum field amplitudes are equal in each cell; that is, the field flatness is 1. However, mechanical errors are unavoidable in the RF gun machining process, leading to a field imbalance between half- and full cells. The influences of field flatness values of 0.9, 1.0, 1.1 on the emittance at 1 nC and 2 nC were studied. The axial field distributions for a photocathode field gradient of 100 MV/m are shown in Fig. 12. The beam dynamics simulation results are presented in Table 5. The results suggest that the field flatness had little influence on the output emittance within the studied range.

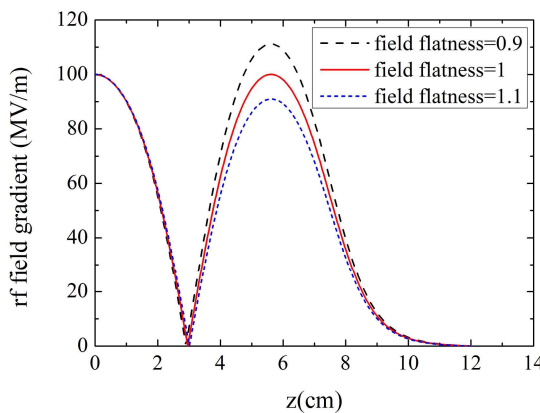


Fig. 12 Axial field distribution with field flatness of 0.9, 1.0, and 1.1

Table 5 Simulation results with 0.9, 1.0, and 1.1 field flatness

Field flatness	0.9	1.0	1.1	0.9	1.0	1.1
Bunch charge (nC)	1	1	1	2	2	2
RMS bunch length (mm)	1.04	1.04	1.03	1.20	1.25	1.21
Output emittance (mm·mrad)	0.65	0.65	0.69	0.92	0.92	0.98

4. Stability analysis

In a photoinjector, component misalignment such as displacement and rotation errors of the gun, traveling wave acceleration cavities, and solenoids may result in emittance growth. The sensitivity of emittance to component misalignment must be known to control these errors within a reasonable range. RF jitter results in beam parameter fluctuations around the set point.

4.1 Mechanical errors

Displacement or rotation errors of the components cause more electrons to be located in the transverse defocusing field; the center of the bunch deviates from the axial focusing magnetic field of the solenoids, leading to transverse emittance growth. Table 6 presents the effects of mechanical errors on the beam emittance at bunch charges of 1 nC and 2 nC. When the beam energy is low, misalignment of the RF gun and solenoids has an obvious influence on the emittance growth; in the higher-energy section, misalignment (within 1 mm or 1 mrad) of the acceleration tubes has a smaller effect on emittance growth.

Table 6 Emittance growth due to misalignment

Parameter	Error value	ε -growth (1 nC)	ε -growth (2 nC)
Cathode	0.1 mm	2.35%	1.55%
Main Solenoid 1	0.2 mm	2.26%	5.32%
Main Solenoid 1	1 mrad	2.56%	3.71%
Solenoid 2	0.2 mm	0.01%	0.01%
Solenoid 2	1 mrad	0.45%	0.03%
TW1	1 mm	0.06%	0.33%
TW1	1 mrad	0.8%	1.08%
TW2	1 mm	0.12%	0.01%
TW2	1 mrad	0.4%	0.44%

4.2 Operation errors

During operation of the photoinjector, parameter jitter affects the normalized transverse emittance, beam size, and beam energy. There were 1000-shot operation parameters considered to simulate the errors with 100k macro-particles tracked while varying bunch charge, laser timing, laser spot size, laser offset, RF phases and amplitudes, and magnetic field strengths. Within each error range, each sample point was selected with the same probability of occurrence, following a uniform distribution, as shown in Table 7. The simulated statistical results for 1 and 2 nC are shown in Figs. 13 and 14, respectively. As long as the parameter errors are controlled in the ranges shown in Table 7, the beam stability of the photoinjector can meet the requirements of the Wuhan Photon Source.

Table 7 Error analysis of operation parameters

Parameter	Jitter
Bunch charge $\Delta Q/Q$ (%)	[-5,5]
Laser timing (fs)	[-100,100]
Laser pulse length (ps)	[-0.5,0.5]
Laser pulse rise/fall time (ps)	[-0.05,0.05]
Laser spot size (%) ^a	[-5,5]
Laser spot offset (%) ^b	[-10,10]
Gun phase (degree)	[-0.1,0.1]
Gun amplitude (%)	[-0.1,0.1]
TW1 and TW2 phase (degree)	[-0.1,0.1]
TW1 and TW2 amplitude (%)	[-0.1,0.1]
Main solenoid1 and solenoid2 $\Delta B/B$ (%)	[-0.1,0.1]

^a Laser spot size jitter is independent in the horizontal and vertical directions

^b Laser spot offset jitter is relative to the optimal RMS laser spot size

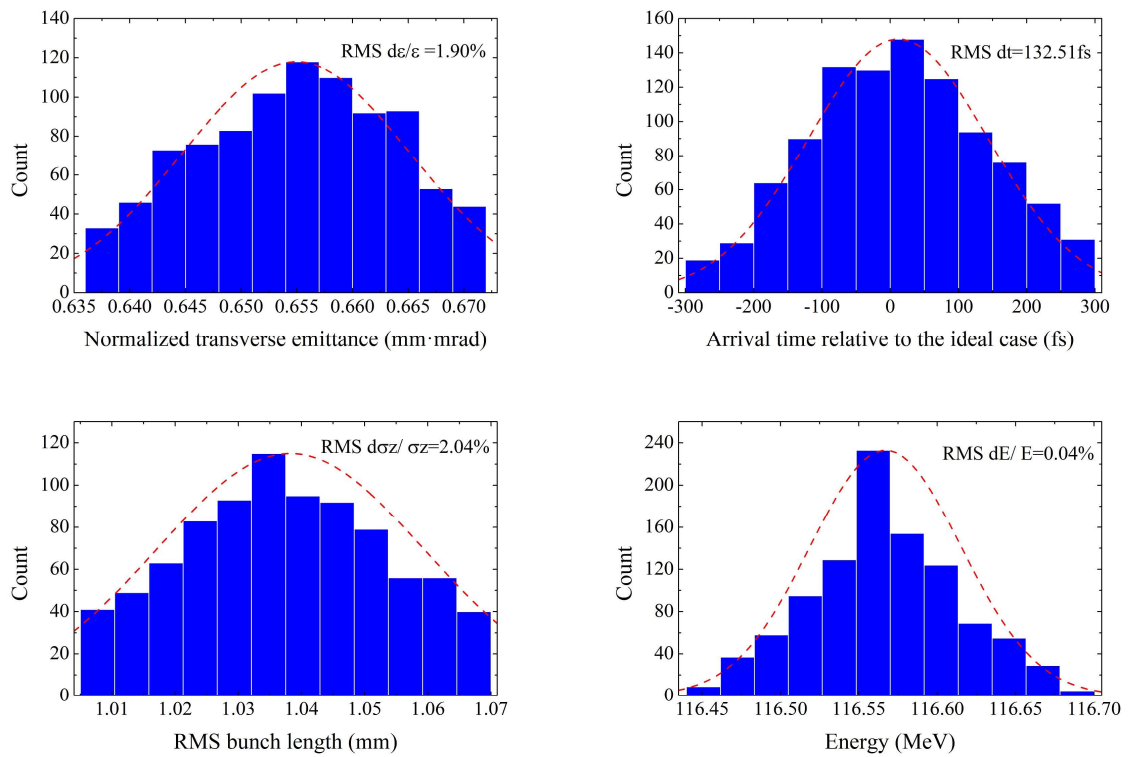


Fig. 13 Influence of parameter jitter on beam with 1-nC bunch charge

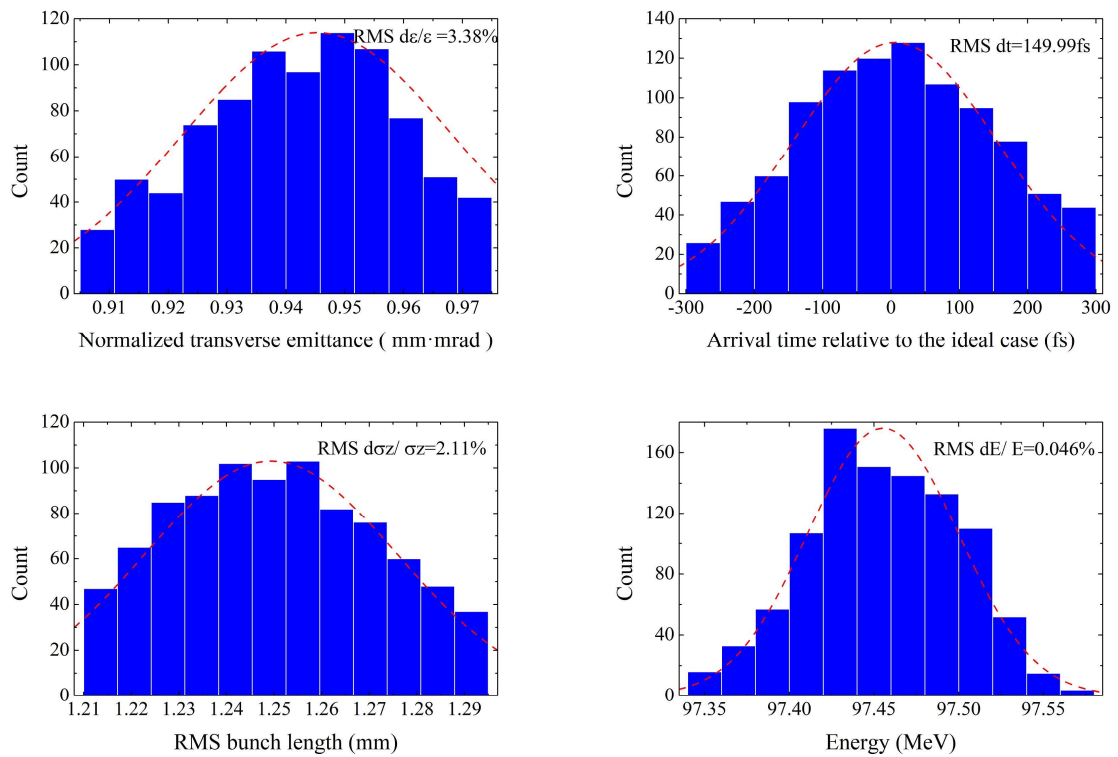


Fig. 14 Influence of parameter jitter on beam with 2-nC bunch charge

5. Results and discussion

This study presents the systematic design of an S-band photoinjector that can provide high-bunch-charge beams for storage rings operating in swap-out injection mode and high brightness beams for FELs. A simulation method coupling ASTRA and NSGAII was developed and demonstrated as an efficient way to obtain the global optimal solution in the beam dynamics design. During the optimization process, the global optimal solution was gradually approached by iteratively narrowing the scanning range. After optimization, when a field gradient of 100 MV/m was selected in the RF gun, the normalized transverse emittance at the exit of the photoinjector reached a value as low as 0.65 and 0.92 mm·mrad at 1 and 2 nC, respectively. At 2 nC, all hardware positions remained the same as the optimal positions that had been determined at 1 nC. The results show that high beam quality including short bunch length and low emittance can be obtained with a large range of bunch charges by simply adjusting the operation parameters of the photoinjector. Moreover, the beam stability analysis of the photoinjector provides theoretical guidance for controlling mechanical and operational errors in an actual system.

Contributions Statement All authors contributed to the study conception and design. Material preparation, data collection and analysis were performed by Ze-Yi Dai, Yuan-Cun Nie, Zi Hui, Lan-Xin Liu and Zi-Shuo Liu. The first draft of the manuscript was written by Ze-Yi Dai and all authors commented on previous versions of the manuscript. All authors read and approved the final manuscript.

References

1. M. Eriksson, J.F. van der Veen, C. Quitmann et al., Diffraction-limited storage rings—a window to the science of tomorrow. *J. Synchrotron Rad.* **21**, 837–842 (2014). <https://doi.org/10.1107/S1600577514019286>
2. A. Bjorling, S. Kalbfleisch, M. Kahnt et al., Ptychographic characterization of a coherent nanofocused X-ray beam. *Opt. Express* **28**, 5069–5076 (2020). <https://doi.org/10.1364/OE.386068>
3. S. Kumar, Next Generation Light Sources and Applications. [arXiv:1807.11084v3](https://arxiv.org/abs/1807.11084v3)
4. C. Bostedt, S. Boutet, D.M. Fritz et al., LINAC coherent light source: the first five years. *Rev. Mod. Physics* **88**, 015007 (2016). <https://doi.org/10.1103/RevModPhys.88.015007>
5. C. Feng, H.X. Deng, Review of fully coherent free-electron lasers. *Nucl. Sci. Tech.* **29**, 160 (2018). <https://doi.org/10.1007/s41365-018-0490-1>
6. Z. Zhao, D. Wang, Q. Gu et al., SXFEL: A Soft X-ray free electron laser in China. *Synchrotron Rad. News* **30**, 29–33 (2017). <https://doi.org/10.1080/08940886.2017.1386997>

7. L.M. Zheng, Y.C. Du, Z. Zhang et al., Development of S-band photocathode RF guns at Tsinghua University. *Nucl. Instrum. Meth. Phys. Res. Sect. A* **834**, 98–107 (2016). <https://doi.org/10.1016/j.nima.2016.07.015>
8. P. Emma, R. Akre, J. Arthur et al., First lasing and operation of an ångstrom-wavelength free-electron laser. *Nat. Photonics* **4**, 641–647 (2010). <https://doi.org/10.1038/nphoton.2010.176>
9. H.S. Kang, C.K. Min, H. Heo et al., Hard X-ray free-electron laser with femtosecond-scale timing jitter. *Nat. Photonics* **11**, 708–713 (2017). <https://doi.org/10.1038/s41566-017-0029-8>
10. J. Lee, I.S. Ko, J.H. Han et al., Parameter optimization of PAL-XFEL injector. *J. Korean Phys. Soc.* **72**, 1158–1165 (2018). <https://doi.org/10.3938/jkps.72.1158>
11. C. Milne, T. Schietinger, M. Aiba et al., SwissFEL: the Swiss X-ray free electron laser. *Appl. Sci.* **7**, 720 (2017). <https://doi.org/10.3390/app7070720>
12. T. Schietinger, M. Pedrozzi, M. Aiba et al., Commissioning experience and beam physics measurements at the SwissFEL injector test facility. *Phys. Rev. Accel. Beams* **19**, 100702 (2016). <https://doi.org/10.1103/PhysRevAccelBeams.19.100702>
13. M. Bei, M. Borland, Y. Cai et al., The potential of an ultimate storage ring for future light sources. *Nucl. Instru. Meth. Phys. Res. Sect. A* **622**, 518–535 (2010). <https://doi.org/10.1016/j.nima.2010.01.045>
14. P.F. Tavares, E. Al-Dmour, A. Andersson et al., Commissioning and first-year operational results of the MAX IV 3 GeV ring. *J. Synchrotron Rad.* **25**, 1291–1316 (2018). <https://doi.org/10.1107/S1600577518008111>
15. K. Duhrkop, M. Fleischauer, M. Ludwig et al., SIRIUS 4: a rapid tool for turning tandem mass spectra into metabolite structure information. *Nat. Methods* **16**, 299–302 (2019). <https://doi.org/10.1038/s41592-019-0344-8>
16. R. Hettel, DLSR design and plans: an international overview. *J. Synchrotron Rad.* **21**, 843–855 (2014). <https://doi.org/10.1107/S1600577514011515>
17. Y.C. Nie, C. Liebig, M. Hüning et al., Tuning of 2.998 GHz S-band hybrid buncher for injector upgrade of LINAC II at DESY. *Nucl. Instru. Meth. Phys. Res. Sect. A* **761**, 69–78 (2014). <https://doi.org/10.1016/j.nima.2014.05.043>
18. J. Andersson, F. Curbis, L. Isaksson et al., The Pre-Injector and Photocathode Gun Design for the MAX IV SXL. in *Proceedings of IPAC2019*, Melbourne, Australia, 2064–2066 (2019)
19. W.X. Wang, C. Li, Z.G. He, et al., Commissioning the photocathode radio frequency gun: a candidate electron source for Hefei Advanced Light Facility. *Nucl. Sci. Tech.* **33**, 1–9 (2022). <https://doi.org/10.1007/s41365-022-01000-6>
20. Y. Jiao, G. Xu, X.H. Cui et al., The HEPS project. *J. Synchrotron Rad.* **25**, 1611–1618 (2018). <https://doi.org/10.1107/S1600577518012110>
21. S. Henderson, Status of the APS upgrade project. in *Proceedings of IPAC 2015*, Richmond, VA, USA, 1791–1793 (2015)
22. D. Wang, K.L.F. Bane, S. Santis et al., Single bunch instability simulations in the storage ring of the ALS-U project. in *Proceedings of IPAC2021*, Campinas, SP, Brazil, 2783–2785 (2021)

23. L. Yang, D. Robin, F. Sannibale et al., Global optimization of an accelerator lattice using multiobjective genetic algorithms. *Nucl. Instru. Meth. Phys. Res. Sect. A* **609**, 50–57 (2009). <https://doi.org/10.1016/j.nima.2009.08.027>
24. J. Wan, P. Chu, Y. Jiao, Neural network-based multiobjective optimization algorithm for nonlinear beam dynamics. *Phys. Rev. Accel. Beams* **23**, 081601 (2020). <https://doi.org/10.1103/PhysRevAccelBeams.23.081601>
25. C. Meng, O.Z. Xiao, S.L. Pei et al., Optimization of Klystron efficiency with MOGA. in Proceedings of IPAC2018, Vancouver, BC, Canada, 2419–2421 (2018)
26. X. Pang, L.J. Rybarczyk, Multi-objective particle swarm and genetic algorithm for the optimization of the LANSCE linac operation. *Nucl. Instru. Meth. Phys. Res. Sect. A* **741**, 124–129 (2014). <https://doi.org/10.1016/j.nima.2013.12.042>
27. H. Feng, S. De Santis, K. Baptiste et al., Proposed design and optimization of a higher harmonic cavity for ALS-U. *Rev. Sci. Instr.* **91**, 014712 (2020). <https://doi.org/10.1063/1.5135955>
28. R. Bartolini, M. Apollonio, I.P.S. Martin, Multiobjective genetic algorithm optimization of the beam dynamics in LINAC drivers for free electron lasers. *Phys. Rev. ST Accel. Beams* **15**, 030701 (2012). <https://doi.org/10.1103/PhysRevSTAB.15.030701>
29. C. Gulliford, A. Bartnik, I. Bazarov et al., Multiobjective optimization design of an RF gun based electron diffraction beam line. *Phys. Rev. Accel. Beams* **20**, 033401 (2017). <https://doi.org/10.1103/PhysRevAccelBeams.20.033401>
30. I.V. Bazarov, C.K. Sinclair, Multivariate optimization of a high brightness dc gun photoinjector. *Phys. Rev. ST Accel. Beams* **8**, 034202 (2005). <https://doi.org/10.1103/PhysRevSTAB.8.034202>
31. K. Deb, A fast and elitist multiobjective genetic algorithm: NSGA-II. *IEEE trans. Evol. Comput.* **6**, 182–197 (2002). <https://doi.org/10.1109/4235.996017>
32. J. Rosenzweig, S. Anderson, K. Bishofberger et al., The neptune photoinjector. *Nucl. Instru. Meth. Phys. Res. Sect. A* **410**, 437–451 (1998). [https://doi.org/10.1016/S0168-9002\(98\)00175-2](https://doi.org/10.1016/S0168-9002(98)00175-2)
33. K. Halbach, R. Holsinger, Superfish—a computer program for evaluation of RF cavities with cylindrical symmetry. *Particle Accel.* **7**, 213–222 (1976)
34. T. Rao, D.H. Dowell, An engineering guide to photoinjectors. *arXiv:1403.7539v1*
35. C. Limborg-Deprey, L. Xiao, D. Dowell et al., Modifications on RF components in the LCLS injector. in Proceedings of PAC2005, Knoxville, Tennessee, 2233–2235 (2005)
36. D. Alesini, A. Battisti, M. Bellaveglia et al., Design, realization, and high power test of high gradient, high repetition rate brazing-free S-band photogun. *Phys. Rev. Accel. Beams* **21**, 112001 (2018). <https://doi.org/10.1103/PhysRevAccelBeams.21.112001>
37. K. Flöttmann: ASTRA: A space charge tracking algorithm, <http://www.desy.de/~mpyflo/>
38. B.E. Carlsten, New photoelectric injector design for the Los Alamos National Laboratory XUV FEL accelerator. *Nucl. Instru. Meth. Phys. Res. Sect. A* **285**, 313–319 (1989). [https://doi.org/10.1016/0168-9002\(89\)90472-5](https://doi.org/10.1016/0168-9002(89)90472-5)
39. Y. Ding, A. Brachmann, F.J. Decker et al., Measurements and simulations of ultralow emittance and ultrashort electron beams in the LINAC coherent light source. *Phys. Rev. Lett.* **102**, 254801 (2009). <https://doi.org/10.1103/PhysRevSTAB.15.030701>

40. P.W. Huang, H. Qian, Y. Du et al., Photoemission and degradation of semiconductor photocathode. *Phys. Rev. Accel. Beams* **22**, 123403 (2019).
<https://doi.org/10.1103/PhysRevAccelBeams.22.123403>
41. F. Zhou, A. Brachmann, P. Emma et al., Impact of the spatial laser distribution on photocathode gun operation. *Phys. Rev. ST Accel. Beams* **15**, 090701 (2012).
<https://doi.org/10.1103/PhysRevSTAB.15.090701>
42. S. Lederer, S. Schreiber, Cs₂Te photocathode lifetime at flash and European XFEL. in Proceedings of IPAC2018, Vancouver, BC, Canada, 2496–2498 (2018)
43. D.H. Dowell, J.F. Schmerge, Quantum efficiency and thermal emittance of metal photocathodes. *Phys. Rev. ST Accel. Beams* **12**, 074201 (2009).
<https://doi.org/10.1103/PhysRevSTAB.12.074201>
44. H.H. Li, J. Wang, L. Tang et al., Project of Wuhan photon source. in Proceedings of IPAC2021, Campinas, SP, Brazil, 346–349 (2021)
45. J.K. Kim, RF and space-charge effects in laser-driven RF electron guns. *Nucl. Instru. Meth. Phys. Res. Sect. A* **275**, 201–218 (1989).
[https://doi.org/10.1016/0168-9002\(89\)90688-8](https://doi.org/10.1016/0168-9002(89)90688-8)
46. E. Pirez, P. Musumeci, J. Maxson et al., S-band 1.4 cell photoinjector design for high brightness beam generation. *Nucl. Instru. Meth. Phys. Res. Sect. A* **865**, 109–113 (2017).
<https://doi.org/10.1016/j.nima.2016.08.063>